SISSA

Antiproton tagging and vertex fitting in a Timepix3 detector

To cite this article: S. Aghion *et al* 2018 *JINST* **13** P06004

View the article online for updates and enhancements.

Related content

- Measurement of antiproton annihilation on Cu, Ag and Au with emulsion films
  S. Aghion, C. Amsler, A. Ariga et al.

- Prospects for measuring the gravitational free-fall of antihydrogen with emulsion detectors
  S Aghion, O Ahlén, C Amsler et al.

- Detection of low energy antiproton annihilations in a segmented silicon detector
  S Aghion, O Ahlén, A S Belov et al.

IOP ebooks™

Bringing you innovative digital publishing with leading voices to create your essential collection of books in STEM research.

Start exploring the collection - download the first chapter of every title for free.

Antiproton tagging and vertex fitting in a Timepix3 detector

The AEgIS collaboration

S. Aghion,[a,b] C. Amsler,[c] M. Antonello,[b,d] A. Belov,[t] G. Bonomi,[f,g] R.S. Brusa,[h,i]
M. Caccia,[b,d] A. Camper,[j] R. Caravita,[j] F. Castelli,[b,k] G. Cerchiari,[l] D. Comparat,[m]
G. Consolati,[n,b] A. Demetrio,[o] L. Di Noto,[p,q] M. Doser,[j] C. Evans,[a,b] M. Fanì,[p,q,j]
R. Ferragut,[a,b] J. Fesel,[j] A. Fontana,[g] S. Gerber,[j] M. Giammarchi,[b] A. Gligorova,[c]
F. Guatieri,[h,i] Ph. Hackstock,[c] S. Haider,[j] A. Hinterberger,[j] H. Holmestad,[r,1] A. Kellerbauer,[l]
O. Khalidova,[j] D. Krasnický,[q] V. Lagomarsino,[p,q] P. Lansonneur,[s] P. Lebrun,[s]
C. Malbrunot,[j,c] S. Mariazzi,[i] J. Marton,[c] V. Matveev,[t,e] S.R. Müller,[o] G. Nebbia,[u] P. Nedelec,[s]
M. Oberthaler,[o] N. Pacifico,[v,j] D. Pagano,[f,g] L. Penasa,[h,i] V. Petracek,[w] F. Prelz,[b]
M. Prevedelli,[x] B. Rienaecker,[j] J. Robert,[m] O.M. Røhne,[r] A. Rotondi,[g,y] H. Sandaker,[r]
R. Santoro,[b,d] L. Smestad,[j,z] F. Sorrentino,[p,q] G. Testera,[q] I. C. Tietje,[j] E. Widmann,[c]
P. Yzombard,[l] C. Zimmer,[j,l,aa] J. Zmeskal[c] and N. Zurlo[g,ab]

[a]*LNESS, Department of Physics, Politecnico di Milano, via Anzani 42, 22100 Como, Italy*

[b]*INFN Milano, via Celoria 16, 20133 Milano, Italy*

[c]*Stefan Meyer Institute for Subatomic Physics, Austrian Academy of Sciences,*
Boltzmanngasse 3, 1090 Vienna, Austria

[d]*Department of Science, University of Insubria, Via Valleggio 11, 22100 Como, Italy*

[e]*Joint Institute for Nuclear Research, Dubna 141980, Russia*

[f]*Department of Mechanical and Industrial Engineering, University of Brescia,*
via Branze 38, 25123 Brescia, Italy

[g]*INFN Pavia, via Bassi 6, 27100 Pavia, Italy*

[h]*Department of Physics, University of Trento, via Sommarive 14, 38123 Povo, Trento, Italy*

[i]*TIFPA/INFN Trento, via Sommarive 14, 38123 Povo, Trento, Italy*

[j]*Physics Department, CERN, 1211 Geneva 23, Switzerland*

[k]*Department of Physics, University of Milano, via Celoria 16, 20133 Milano, Italy*

[l]*Max Planck Institute for Nuclear Physics, Saupfercheckweg 1, 69117 Heidelberg, Germany*

[m]*Laboratoire Aimé Cotton, Université Paris-Sud, ENS Paris Saclay, CNRS, Université Paris-Saclay,*
91405 Orsay Cedex, France

[n]*Department of Aerospace Science and Technology, Politecnico di Milano,*
via La Masa 34, 20156 Milano, Italy

[1]Corresponding author.

https://doi.org/10.1088/1748-0221/13/06/P06004

^{o} *Kirchhoff-Institute for Physics, Heidelberg University,*
  Im Neuenheimer Feld 227, 69120 Heidelberg, Germany

^{p} *Department of Physics, University of Genova, via Dodecaneso 33, 16146 Genova, Italy*

^{q} *INFN Genova, via Dodecaneso 33, 16146 Genova, Italy*

^{r} *Department of Physics, University of Oslo, Sem Sælandsvei 24, 0371 Oslo, Norway*

^{s} *Institute of Nuclear Physics, CNRS/IN2p3, University of Lyon 1, 69622 Villeurbanne, France*

^{t} *Institute for Nuclear Research of the Russian Academy of Science, Moscow 117312, Russia*

^{u} *INFN Padova, via Marzolo 8, 35131 Padova, Italy*

^{v} *Institute of Physics and Technology, University of Bergen, Allégaten 55, 5007 Bergen, Norway*

^{w} *Czech Technical University, Prague, Brehová 7, 11519 Prague 1, Czech Republic*

^{x} *University of Bologna, Viale Berti Pichat 6/2, 40126 Bologna, Italy*

^{y} *Department of Physics, University of Pavia, via Bassi 6, 27100 Pavia, Italy*

^{z} *The Research Council of Norway, P.O. Box 564, 1327 Lysaker, Norway*

^{aa} *Department of Physics, Heidelberg University, Im Neuenheimer Feld 226, 69120 Heidelberg, Germany*

^{ab} *Department of Civil, Environmental, Architectural Engineering and Mathematics, University of Brescia,*
  via Branze 43, 25123 Brescia, Italy

E-mail: helga.holmestad@cern.ch

ABSTRACT: Studies of antimatter are important for understanding our universe at a fundamental level. There are still unsolved problems, such as the matter-antimatter asymmetry in the universe. The AEgIS experiment at CERN aims at measuring the gravitational fall of antihydrogen in order to determine the gravitational force on antimatter. The proposed method will make use of a position-sensitive detector to measure the annihilation point of antihydrogen. Such a detector must be able to tag the antiproton, measure its time of arrival and reconstruct its annihilation point with high precision in the vertical direction.

This work explores a new method for tagging antiprotons and reconstructing their annihilation point. Antiprotons from the Antiproton Decelerator at CERN were used to obtain data on direct annihilations on the surface of a silicon pixel sensor with Timepix3 readout. These data were used to develop and verify a detector response model for annihilation of antiprotons in this detector. Using this model and the antiproton data it is shown that a tagging efficiency of $50 \pm 10\%$ and a vertical position resolution of $22 \pm 0.5 \, \mu$m can be obtained.

Contents

1   Introduction

The main goal of the AEgIS experiment [1, 2] is to measure the gravitational force on antihydrogen to test the weak equivalence principle for antimatter. The method proposed is to accelerate a cold, pulsed beam of antihydrogen in an inhomogenous electric field (Stark acceleration). The beam is then sent through a classical moiré deflectometer [3, 4], as seen in figure 1. The antiatoms passing through the gratings annihilate on a position-sensitive detector, forming a fringe pattern. The gravitational acceleration can be observed by measuring the downward or upward shift of this pattern compared to a path undeflected in the vertical direction. The position-sensitive detector must be able to tag antihydrogen atoms, reconstruct their annihilation point, and measure their time of flight through the moiré deflectometer. Assuming a velocity of 500 m/s for the antihydrogen and a flight path of 1.0 m, a vertical fall of $\approx 20\,\mu$m is expected [5].

Antiproton annihilations as studied here can also be used for studying antihydrogen annihilations, as the positron annihilates independently on an atomic electron, resulting in two 511 keV

photons, to which a silicon detector is not sensitive. Previous studies have been able to describe and identify signatures of antiproton annihilations in detectors, and to make a comparison between data and simulations [6, 7].

This study is the first in which quantitative results are found for the tagging efficiency and the position resolution of annihilations in a silicon pixel detector equipped with the Timepix3 [8] readout. The results provide the background for evaluating the usability of such a detector in AEgIS and other antimatter experiments.
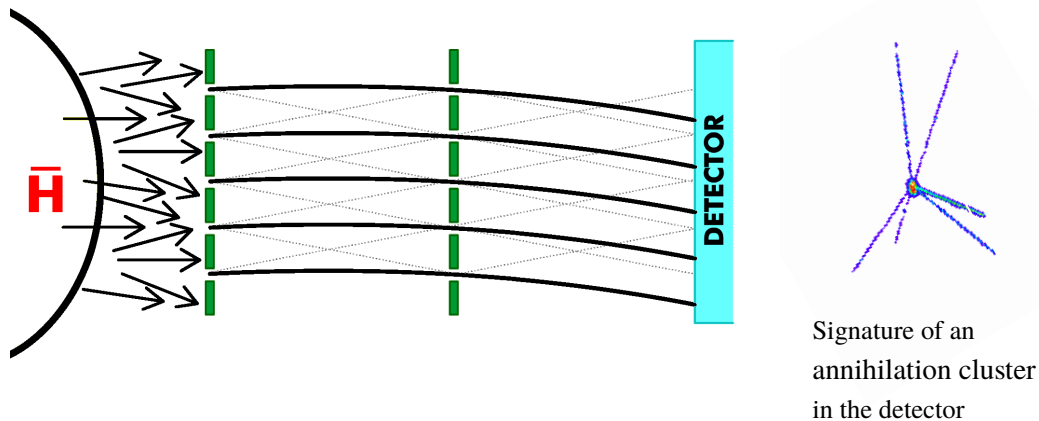

Figure 1. Illustration of the trajectories of antihydrogen passing through a classical moiré deflectometer. The antihydrogen atoms annihilate directly in the detector, and star-shaped annihilation clusters are detected. The paths of antihydrogen through the deflectometer are deflected by the gravitational field.

1.1 The GRACE beamline

The experimental setup is situated on the GRACE beamline [9] at the Antiproton Decelerator (AD) at CERN, where approximately 3×10^7 antiprotons with a kinetic energy of 5.3 MeV are delivered from the AD every ≈ 100 seconds [10]. Figures 2 and 3 show an illustration and a photo of the setup, while figure 4 shows the Timepix3 detector mounted in GRACE.

The GRACE beamline is designed to provide antiprotons with kinetic energies below 15 keV, while minimizing the background produced by antiprotons annihilating without reaching the detector. The beamline consists of a vacuum chamber with an extraction line inclined by 40° with respect to the incident beam. A 25 μm thick circular titanium window with a diameter of 40.0 mm allows the antiprotons to enter into GRACE. Einzel lenses for focusing and a pair of bending electrodes guide the low-energy antiprotons towards the detector. To further reduce the energy of the beam, an aluminum degrader of variable thickness is placed in the air gap between the AD and the GRACE beamline.

The degrader thickness and the electrode voltages were manually tuned to achieve the maximum number of star-shaped clusters on the detector. The optimum was found to be with a 33 μm thick aluminum degrader, a bending voltage between 3000 and 4000 V, and a focusing voltage between 3000 and 4000 V on each of the einzel lenses. This configuration was used for the present study.
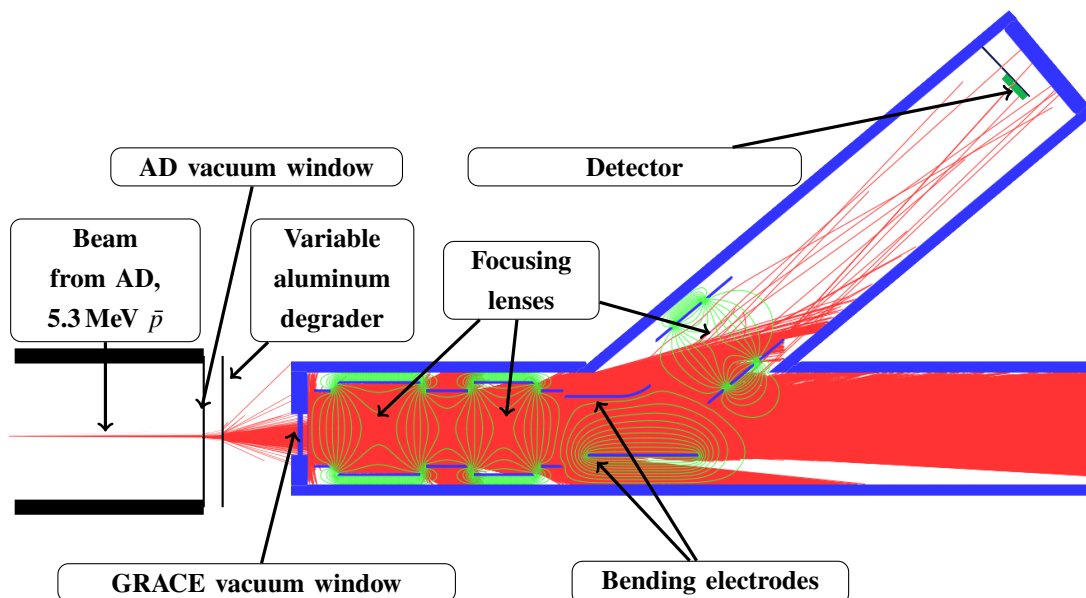
Figure 2. Sketch of the GRACE beamline. The antiproton beam of 5.3 MeV arrives from the AD, loses energy and is scattered by the vacuum windows, the variable degrader, and the air gap between the AD and GRACE. The bending electrodes are used to select antiprotons with energies below 15 keV and direct them towards the detector. The figure is not to scale.
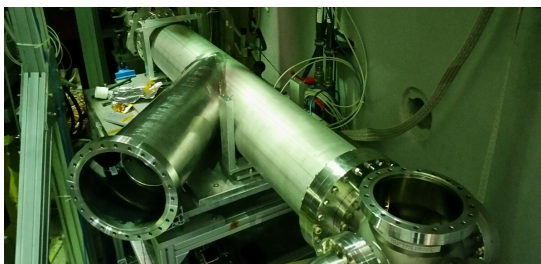

Figure 3. The GRACE beamline at the end of one of the extraction points of the AD before the detector chamber is mounted. The detector chamber is installed on the open flange on the left.

Figure 4. The Timepix3 detector mounted at the end of the GRACE beamline, with the sensor in the center left of the PCB.

1.2 Characteristics of antiproton annihilations in matter

An antiproton annihilation with an atomic nucleon creates on average in total 5 pions (charged and neutral) per annihilation [11]. Some of these pions are likely to penetrate the affected nucleus, and nuclear fragments can break off. The multiplicity and energy distribution of these annihilation products is not fully known. Since simulations are based upon theoretical models and sparse data, they are not able to completely reproduce experimental results. Studies of antiproton annihilations in copper, silver and gold [12] show that the simulation software FLUKA performs better than other available software such as Geant4, and FLUKA was therefore used for this study.

The annihilation products acquire kinetic energy from the mass-to-energy conversion of the annihilation, and travel away from the annihilation point. This gives rise to a star-shaped cluster in the detector, as seen in figure 1. Figure 5 shows the multiplicity of the charged pions and fragments when antiprotons annihilate in aluminum as simulated with FLUKA [13].

The AD delivers around 3×10^7 antiprotons per bunch, and around 20–30 of these antiprotons reach the detector. In addition to the antiprotons, fragments and pions from annihilations occurring in the vacuum window of GRACE, and on the walls and electrodes inside GRACE can also reach the detector. These particles create secondary clusters which contaminate the data. Secondary clusters are defined as clusters caused by nuclear fragments or pions originating from annihilations taking place elsewhere than in the detector itself. Annihilation clusters are defined as clusters caused by antiprotons annihilating directly on the surface of the detector. An annihilation cluster can be recognized as a region with high-energy depositions, possibly with tracks originating from its center. These tracks, from here on called prongs, are caused by pions or nuclear fragments traveling in the plane of the detector. One clear example of an annihilation cluster is shown in figure 1.

To be able to tag antiprotons, an algorithm to distinguish between annihilation clusters and secondary clusters was developed and will be described in section 5. A perfect distinction is not possible, therefore there will always be a trade-off between the tagging efficiency and the false tagging rate. The false tagging rate is defined as the probability of mistagging a secondary cluster as an annihilation cluster.
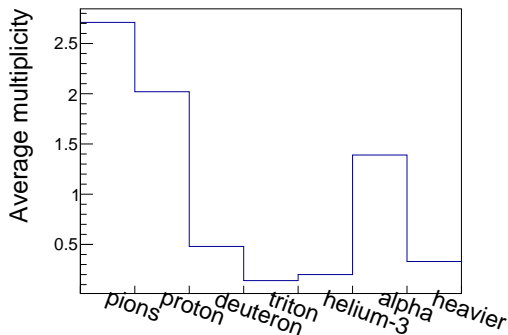

Figure 5. Multiplicity of charged nuclear fragments and pions from antiproton annihilations in aluminum, as simulated with FLUKA [13].
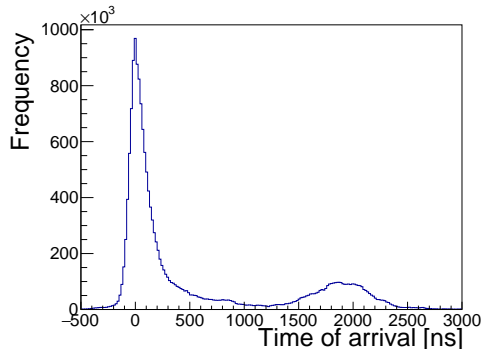

Figure 6. The Time of Arrival (ToA) for all data in the main sample. The antiprotons are found in the second peak.

1.3 The detector

The detector consists of a $675\,\mu\text{m}$ thick silicon sensor with a $0.5\,\mu\text{m}$ thin aluminum layer on top, bump-bonded to an ASIC with the Timepix3 [8] readout. The size of the detector is $14 \times 14\,\text{mm}^2$, with 256×256 pixels and a pixel pitch of $55\,\mu\text{m}$. Each pixel is self-triggering and able to simultaneously measure both Time of Arrival (ToA) and Time over Threshold (ToT). The time resolution is 1–2 ns. The conversion between ToT and deposited energy is found by injecting test pulses into the readout electronics and assuming 3.6 eV as the average energy required to create an electron/hole pair. The depletion voltage was measured to be around 200 V [14], and the device

was operated at this bias voltage during data taking. A photo of the Timepix3 detector is shown in figure 4. The dead time of the pixels is given as the ToT pulse time +475 ns [8]. Experimentally it was observed that the majority of the pixels recover after around 550 ns.

When hit by an antiproton or a heavy nuclear fragment, the detector suffers from the volcano effect [15]. This is a disturbance in the readout when a pixel experiences a large charge readout. Instead of the actual energy deposition, a lower random energy deposition is recorded. Tests with high-energy ions impacting a silicon detector with the Timepix3 readout [16] showed that the transformation from registered ToT to deposited energy breaks down from around 450 keV deposited energy per pixel. The per-pixel highest deposited energy in each cluster seems to follow a Gaussian-like distribution with mean approximately 500 keV and standard deviation approximately 50 keV.

The settings applied to GRACE ensure that all antiprotons to be studied have a kinetic energy below 15 keV. The penetration depth in aluminum at this energy is 0.1 μm [17], therefore the annihilations occur in the top of the 0.5 μm thick aluminum layer on the surface of the sensor.

2 Analysis of experimental data

Two data samples were collected during the test beams in 2015 and 2016, and consisted of one main data sample and one reference data sample. The main sample was taken using the optimal GRACE settings described in section 1.1, and consists of 560 bunches from the AD, each containing a mixture of annihilation clusters and secondary clusters. In this data set 44 bunches are reserved as training data to develop the algorithms for clustering and characterization. The reference data sample was taken with the detector rotated such that its back was facing the beam. In this configuration no antiprotons annihilate directly on the detector. The reference data sample therefore consists of 1561 bunches only containing secondary clusters.

2.1 Time selection

The pions and nuclear fragments from an annihilation have much higher kinetic energy than the antiprotons which are bent towards the detector. According to FLUKA their average kinetic energy is 90 MeV, while the antiprotons bent towards the detector always have a kinetic energy below 15 keV. Therefore a shower of pions and nuclear fragments from annihilations upstream of the detector will hit the detector before the antiprotons. Figure 6 shows the ToA distribution in the main sample, in which two clear peaks can be identified. The first peak is caused by annihilations in the entrance window to GRACE, and consist of pions and nuclear fragments only. Within each bunch the maximum of the first peak is used as an estimate for the time the beam enters GRACE. The antiprotons arrive in the second peak, together with pions and nuclear fragments from annihilations taking place closer to the detector. Since antiprotons are primarily found within the second peak, only pixels that are time delayed by more than 1000 ns from when the beam enters GRACE were selected for analysis.

2.2 Removing the halo signal

Figure 7a shows all the raw hits from one bunch in the main data sample after time selection, where it can be seen that areas with high-energy depositions are surrounded by a halo of lower-energy depositions [18]. Figure 7b shows the same frame after a cut at 5 keV measured energy deposition

has been applied to removed these halo hits. The measured energy deposition in the pixels in the halos is usually between 2 and 4 keV. The halo hits are not caused by actual charge collected in the pixel, but are the result of a detector artifact as described in ref. [19]. Therefore a threshold was set to remove all low-energy pixels, as this makes the clusters easier to analyze by reducing the chance of two distinct clusters to overlap.

In order to find a suitable threshold, the behavior of a Minimum Ionizing Particle (MIP) was considered, as any real particle would result in an energy deposition at least equivalent to a MIP. The search distance of the clustering algorithm presented in the next section is large enough to allow two missing pixels next to each other in a cluster. Geometrical considerations show that, for a pixel pitch p, a particle traveling less than $\frac{p}{\sqrt{2}}$ in one pixel it is bound to travel longer in at least one of the neighboring pixels. For a pixel pitch of 55 μm this distance is $\frac{p}{\sqrt{2}}$ = 38.9 μm. Figure 8 shows the simulated energy deposition from a MIP traversing 38.9 μm of silicon, compared to the distribution of the energy deposited in the pixels in the main data sample. As seen from this figure, the deposited energies from a MIP never goes below 5 keV. Setting the threshold at 5 keV will therefore remove the vast majority of the halo hits, while it will never cut off a track caused by a real particle.

2.3 Clustering and cluster characterization

Pixels that are connected to one of their neighbors by less than 20 ns in time and less than 225 μm in distance are defined as a cluster. These parameters were tuned by inspecting the training data set which was excluded from the analysis. The combination of clustering in both time and space has the advantage that clusters overlapping in space can be distinguished if they don't overlap in time. An algorithm to identify the prongs and the center of a cluster was developed and the procedure is described below. Also here reasonable values of the parameters were found by inspecting the training data set that was excluded from the analysis. The flow of the algorithm is shown in figure 9. The algorithm described here makes it possible to identify the amount of energy deposited in the estimated center of the clusters, and to determine the number of prongs in a cluster.

First, a straight line is fitted to the pixels in the cluster, taking the spatial center of the pixel as the point used for fitting. A low χ^2 value on this fit identifies clusters that are just a single track, and therefore any cluster which has a χ^2 value normalized to its degrees of freedom below 1.0 is assumed to have zero prongs. The second step is to estimate the spatial coordinates of the center of the cluster. For each pixel in the cluster the total deposited energy E_{center} in a circular region with a radius of 275 μm from the center of that pixel is calculated. The mass center of the region with the largest E_{center} is used as an estimate for the center of the cluster (x_0, y_0). Pixels within the 275 μm radius around the point (x_0, y_0) are then discarded to make it easier to recognize the prongs in the cluster.

The next step is to use Hough transformations [20] to identify the straight lines of the prongs extending from the center of the clusters with (x_0, y_0) as a fixed point along the path. The number of hit pixels within each circular segment with opening angle 3.6° radiating from the center of the cluster are counted. The segment with the maximum number of pixels gives the direction of the most evident prong. The pixels belonging to a prong are defined as all pixels within ±20° of the prong direction. The pixels belonging to the identified prong are then removed, and the subsequent most evident prong is identified in the same manner. This procedure is repeated until no more prongs consisting of at least 4 pixels are found.
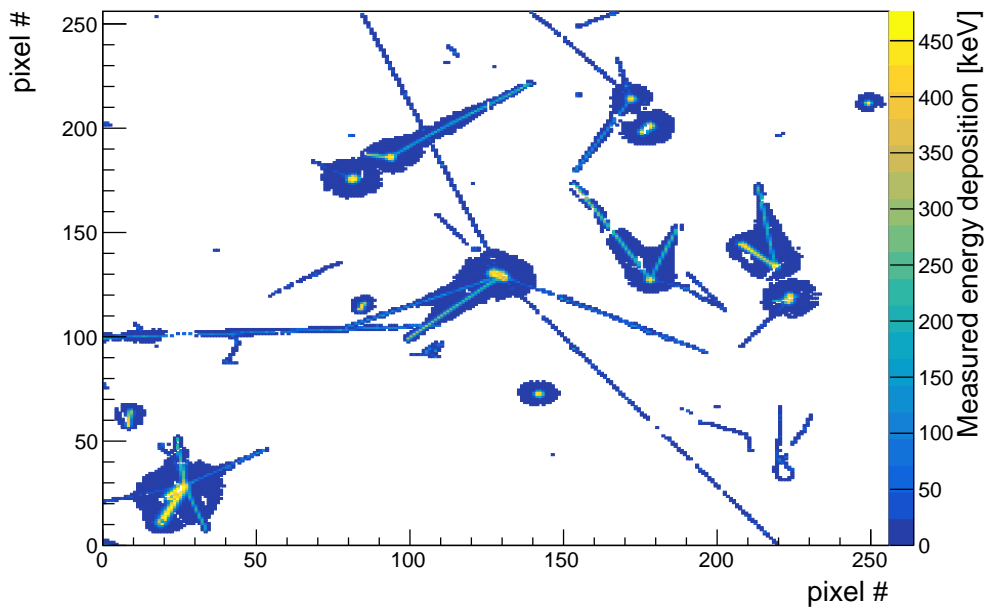
(a) Before the halo hits has been removed.
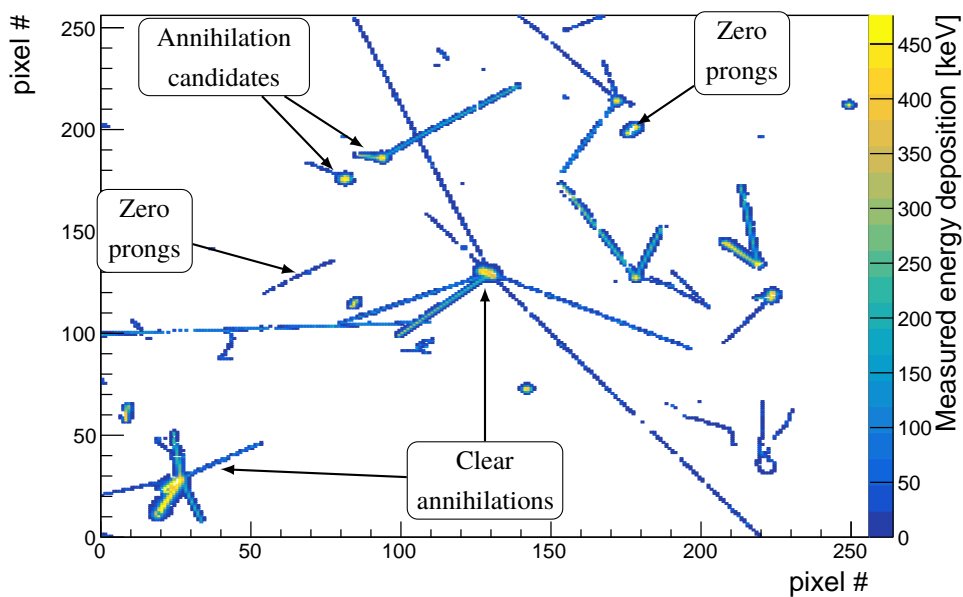
(b) After the halo hits has been removed.

Figure 7. These two frames show all hits from one bunch that are time-delayed by more than 1000 ns from the estimated arrival time into GRACE. Figure a) shows the frame before the halo hits are removed, while figure b) shows the frame after the halo hits are removed.
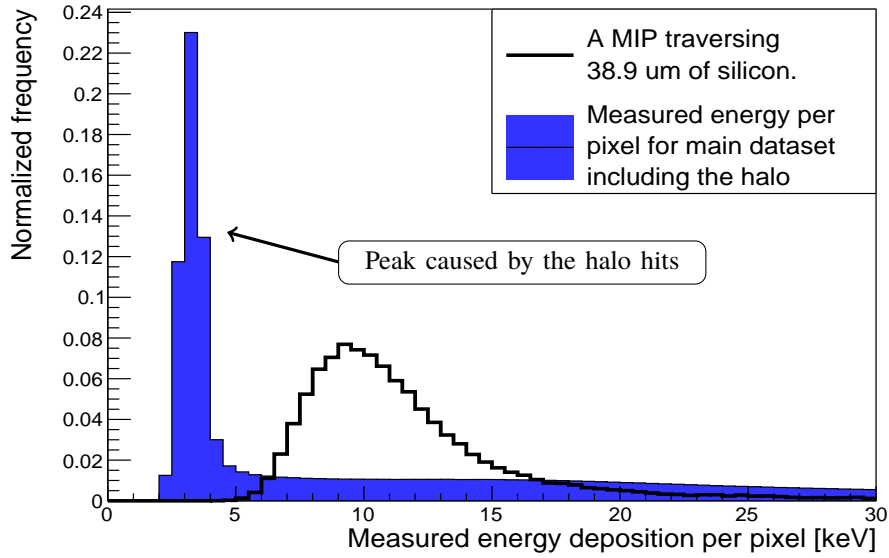
Figure 8. Energy deposition of a MIP (pion of 200 MeV) when traversing 38.9 μm of silicon material, simulated by Geant4, compared to the measured energy depositions in all the pixels in the main data sample.
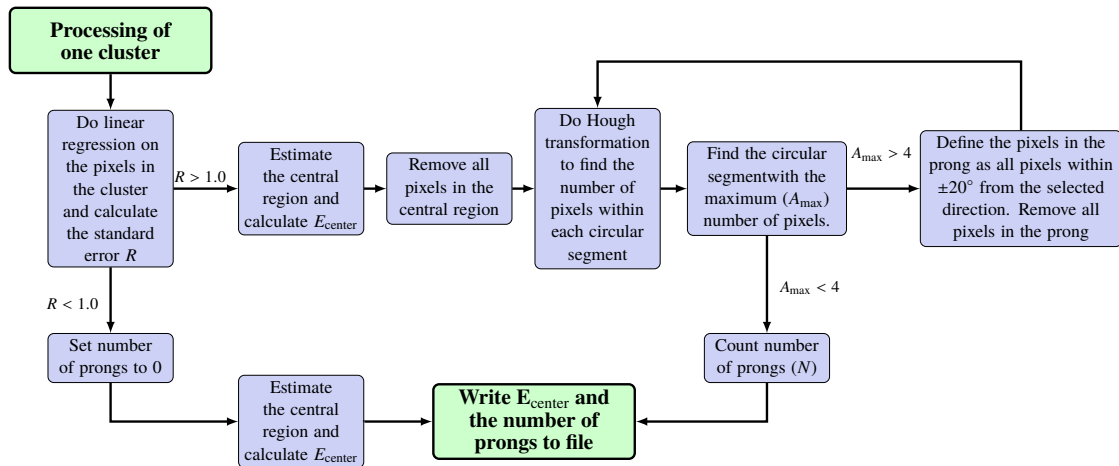

Figure 9. Flow chart for the algorithm developed to characterize the clusters.

3 Detector response model

In order to study the annihilation clusters, a full detector response model based on FLUKA [13] was developed. FLUKA provides the energy deposited in chosen voxels in the detector; for this study the voxels were set to $5.5 \times 5.5 \times 225 \, \mu m^3$ (x × y × depth). Voxels much smaller than the pixel size were chosen in order to take into account the position of the energy deposition within the pixel. This section describes how these raw energy depositions are processed to simulate the detector response. Using the detector response model described here a sample of 10 000 simulated annihilation clusters was produced.

3.1 Modeling charge sharing between pixels

Charges liberated by the energy depositions will diffuse as they drift towards the collecting electrodes, causing charge sharing between pixels. Assuming a Gaussian shape of the charge cloud, its size in terms of the standard deviation at the readout electrodes is

$$\sigma = \sqrt{2Dt_d}, \tag{3.1}$$

where the amount of diffusion depends on the collection time t_d, and the diffusion constant D [21]. A simple model for the collection time is given by

$$t_d = \frac{w^2}{2\mu V_d} \ln\left(1.0 - \frac{z}{w} \cdot \frac{2V_d}{V + V_d}\right), \tag{3.2}$$

where z is the depth of the energy deposition, w the thickness of the detector, V_d the depletion voltage, μ the carrier mobility and V the applied voltage [22, 23].

If the amount of space charge is large enough to disturb the field in the detector the collection time increases. This phenomenon is called the plasma effect [24], and its impact increases with increasing energy deposition. The simple model in equation (3.2) does not consider the plasma effect, however it is included in the device simulation software TCAD [25]. Therefore this software was used to find the collection time for different energy depositions. The simulation was done for three different depths, corresponding to the three different depths of the center of the voxels. The results from the TCAD simulations are found in table 1. For comparison the collection time from the simple model in equation (3.2) is also indicated. There is good agreement between the collection time given by the two models for energy depositions of 1 keV and 10 keV, giving evidence that the plasma effect is not present here. For larger energy depositions, the collection time clearly differs, as expected due to the plasma effect.

The diffusion constant for holes in silicon at room temperature is 12 cm^2/s [26], and this value was used to calculate the charge spread in equation (3.1) when the plasma effect is not present. When the plasma effect is present, the effective diffusion coefficient is found to be 18.0 cm^2/s in silicon at room temperature [24]; this value was therefore used for energy depositions above 10 keV.

The standard deviation σ for the charges liberated in a voxel was found by collecting the energy depositions in the neighborhood of that voxel, and table 1 was then used as a lookup table. The neighborhood is defined by all voxels with their center within a radius of 25 μm, as this is a typical size of the charge cloud. Since the energy deposited can take on continuous values, linear interpolation was used between the values in table 1.

3.2 Modeling front-end electronics effects

In the simulation two front-end electronic effects were taken into account; the volcano effect and suppressed pixels due to the dead time of the pixels. The volcano effect, as described in section 1.3, causes the pixels receiving high-energy depositions to saturate around 500 keV. This effect was taken into account in the simulation by setting all pixels with an energy deposition above 500 keV to a random value following a Gaussian distribution with mean 500 keV and standard deviation 50 keV.

The majority of the pixels in the main data set had a dead time of approximately 550 ns after being hit. The dead time was taken into account by, for each simulated cluster, choosing one

Table 1. Lookup table to find the amount of charge sharing from the energy deposited around the charge that is transported.

Energy deposited	Depth [μm]	Collection time t_c from eq. (3.2) [ns]	Collection time t_c from TCAD [ns]	Calculated σ from TCAD [μm]
1 keV	562.5	45	30	8.5
	337.5	17	14	5.8
	112.5	5	6	3.9
10 keV	562.5	45	36	9.3
	337.5	17	17	6.4
	112.5	5	7	4.1
100 keV	562.5	45	79	16.8
	337.5	17	26	9.6
	112.5	5	16	7.5
1 MeV	562.5	45	349	34.5
	337.5	17	98	18.8
	112.5	5	48	13.0
10 MeV	562.5	45	1780	80.0
	337.5	17	494	42.2
	112.5	5	243	29.6
50 MeV	562.5	45	4584	128.4
	337.5	17	1534	74.3
	112.5	5	760	52.3

random bunch from the experimental main data sample. The pixels in that bunch that are time-delayed between 1350 ns and 1900 ns were set as suppressed in the simulated cluster. This time interval was chosen because the center of the second peak in the ToA distribution in figure 6 is at 1900 ns, indicating the most likely time delay for an antiproton. An antiproton arriving at the most likely time will see all pixels triggered in the chosen time interval as suppressed.

4 Test of the detector response model

The detector response model was verified by comparing the distributions of cluster observables in data and simulation. The observables studied are the cluster size given, the number of prongs, the energy deposited in the center of the cluster and the energy deposited in the whole cluster. The cluster size is defined as the number of pixels making up the clusters after the cut at 5 keV has been applied. The main data sample contains a mixture of secondary clusters and annihilation clusters, while the reference sample contains only secondary clusters. Therefore the main data sample was compared to a weighted combination of the reference data sample and the sample of simulated annihilation clusters. This combined sample of reference data and simulated annihilation clusters was normalized to the total number of clusters in the main data sample.

The fraction of the reference data sample in the combined sample, from here on referred to as r, is a free parameter that was optimized to minimize the χ^2 value of the difference between

the histogram bins. The minimum value for χ^2 was found for $r = 0.83$, and figure 10 shows the comparison between the main data sample and the combined sample using this value for r. For observables relating to the shape of the cluster the agreement between data and simulation is good. There is some discrepancy in the deposited energy, especially in the center of the cluster, as seen in figure 10d. This discrepancy may be caused by inaccuracy in how FLUKA models antiproton annihilations, or in how the volcano effect is modeled, as described in section 3.2. The optimization can also be done on each histogram individually, and the values for r are then 0.81, 0.85, 0.87 and 0.83 for the cluster size, number of prongs, center charge, and total charge, respectively.
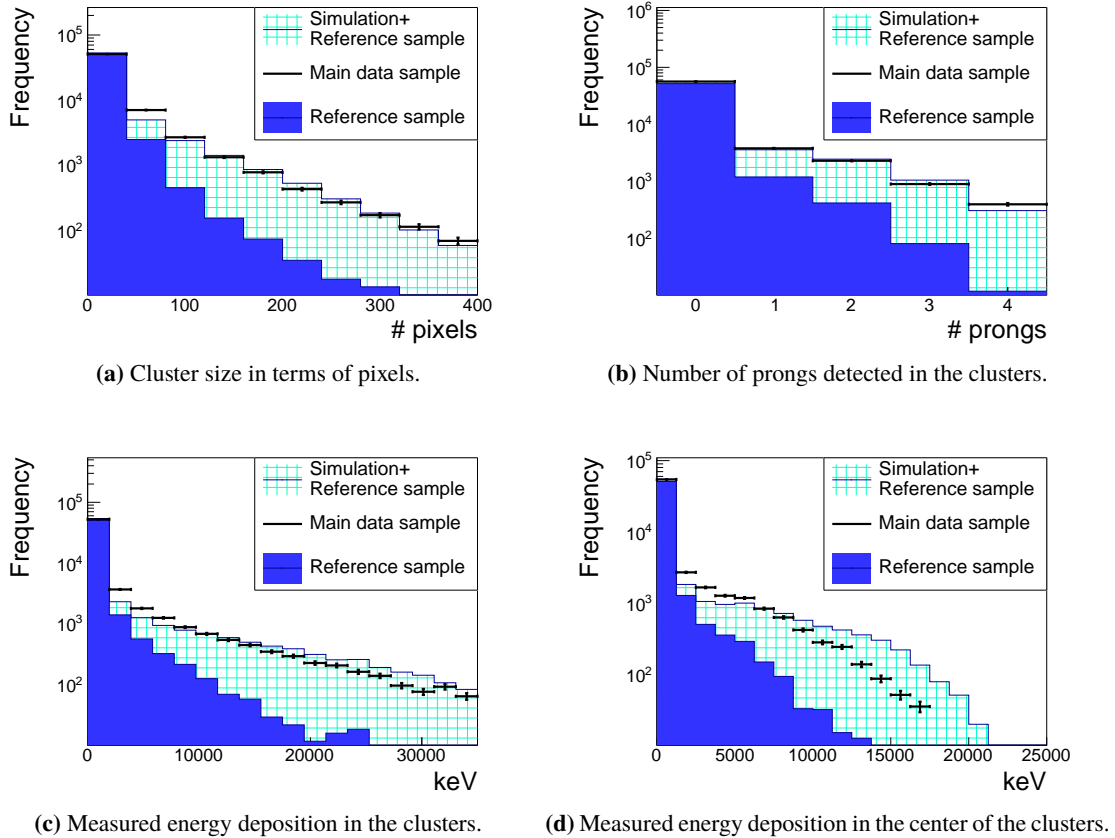

(a) Cluster size in terms of pixels.

(b) Number of prongs detected in the clusters.

(c) Measured energy deposition in the clusters.

(d) Measured energy deposition in the center of the clusters.

Figure 10. Histograms comparing the cluster observables in data and simulations. Observables relating to the shape of the clusters seem to be modeled better. The fraction of secondary clusters is estimated to be $r = 0.83$.

5 Estimate of the tagging efficiency

This section shows how cuts on cluster size and number of prongs are set in order to tag the antiprotons. These two cluster observables were chosen because observables relating to the shape of the clusters are the most accurately modeled ones. The false tagging rate, from here on referred to as p_f, was estimated by the fraction of clusters passing the cuts in the reference data sample. The tagging efficiency, from here on referred to as p_t, was found by applying the cuts on the sample of simulated clusters.
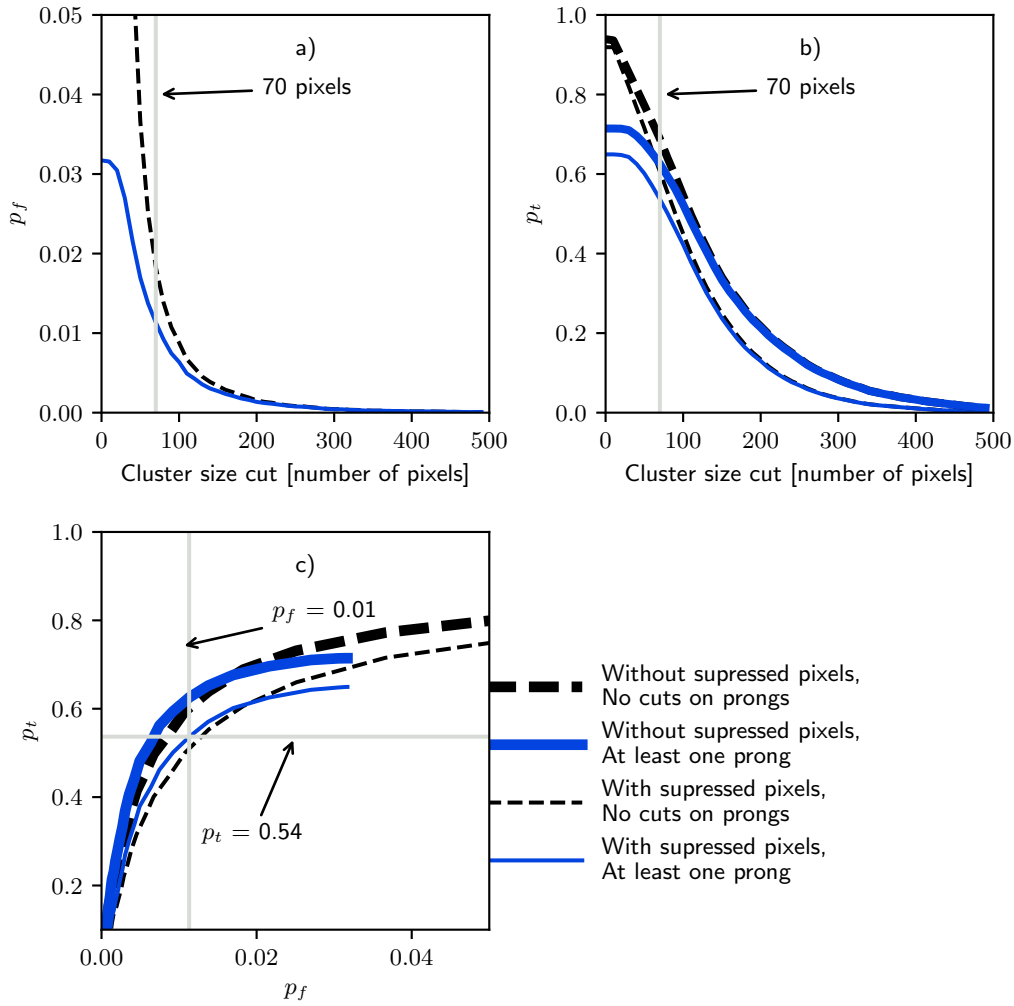
Figure 11. Plots showing the relationship between tagging efficiency (p_t), false tagging rate (p_f) and the cuts. The working cut of 70 pixels, and the resulting efficiency and false tagging rate obtained with this cut and at least one prong are also indicated. **a)** The false tagging rate as a function of the cuts. **b)** The tagging efficiency as a function of the cuts. **c)** The tagging efficiency as a function of the false tagging rate.

Figure 11 shows p_t and p_f as a function of the cuts. The results are shown with and without considering the suppressed pixels in the simulation, as further experiments might be able to reduce the flux and hence avoid suppressed pixels due to dead time. The estimate of p_f always includes suppressed pixels as it is estimated from experimental data. A cut of at least 70 pixels and at least one prong in the cluster gives a tagging efficiency of $p_t = 52\%$. The corresponding value of p_f is then 1.1%, making this cut a good compromise between high tagging efficiency and low false tagging rate. The comparison of the cluster observables after such a cuts is shown in figure 12, and the optimal value for r is then 0.16.

(a) Cluster size in terms of pixels after selection.

(b) Number of prongs detected in clusters after selection.

(c) Measured energy deposition in the clusters after selection.

(d) Measured energy in center of the clusters after selection.
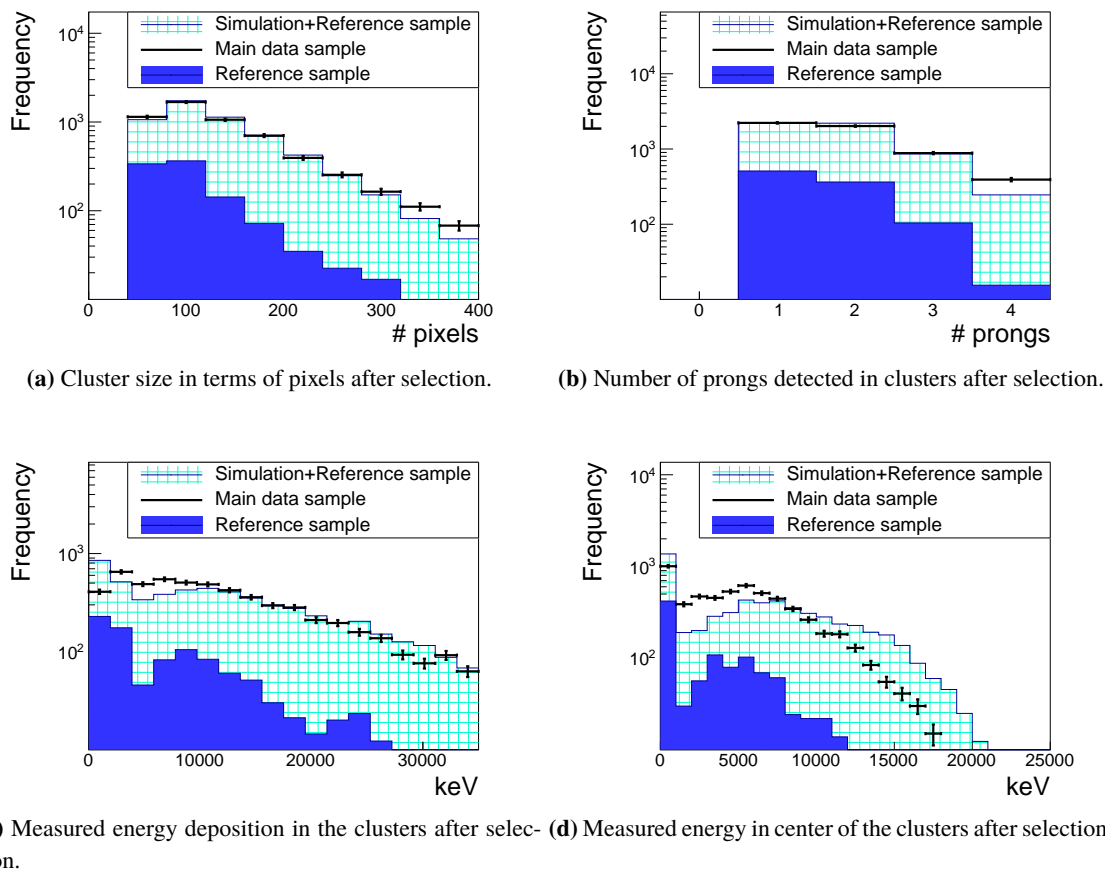
Figure 12. Comparison between data and simulation for clusters passing the cut of at least 70 pixels and at least one prong. As in figure 10 observables related to the shape of the clusters are better modeled. The fraction of secondary clusters is estimated to be 0.18.

5.1 The uncertainty of the tagging efficiency and the false tagging rate

The statistical uncertainty on the tagging efficiency and the false tagging rate depends only on the sample size n and is given by

$$\sigma = \sqrt{\frac{p(1-p)}{n}}, \tag{5.1}$$

where p is the estimated rate. This gives a statistical uncertainty of ±0.5% and ±0.2% for the tagging efficiency and the false tagging rate respectively. However, as seen in figure 10 the simulation does not completely reproduce the data, leaving some discrepancy between data and simulation. This is caused by systematic errors, and two sources of systematic errors were identified. The first being that the reference sample might not completely represent the secondary clusters in the main data sample. The secondary clusters in the main data sample can be caused by annihilations happening anywhere, although solid angle considerations makes it more likely for them to happen close to the detector. In the reference sample the clusters are only caused by annihilations happening downstream of the detector. Therefore secondary clusters in the main sample might be caused by

pions and nuclear fragments impinging more orthogonal to the detector compared to the reference sample. This could cause slightly larger clusters in the reference sample, and therefore the false tagging rate might be overestimated.

The second systematic error concerns how well the simulated clusters reproduce the annihilation clusters in the main sample. To estimate this effect the tagging efficiency was also calculated by a mainly data-driven method. In the main data sample the number of correctly tagged annihilation clusters is given by

$$A_t = N_t - N f p_f, \tag{5.2}$$

where N_t is the number of tagged clusters, N is the total number of clusters, f is the fraction of secondary clusters in the sample, and p_f is again the false tagging rate. The total number of annihilation clusters is

$$A = N - fN. \tag{5.3}$$

The tagging efficiency is estimated by the number of correctly tagged annihilation clusters divided by the total number of annihilation clusters, yielding the following expression for the tagging efficiency:

$$t = \frac{A_t}{A} . \tag{5.4}$$

In the main data sample $N = 63890$, and with the applied cuts of at least 70 pixels and at least one prong $N_t = 5771$. The value of f is unknown, but in section 4 the fraction of secondary clusters was estimated to be in the range of 0.81–0.87. By equation (5.4) this corresponds to a tagging efficiency between 38% and 56%.

This method of calculating the tagging efficiency includes the false tagging rate that might be overestimated. However, the effect is not severe. Setting the tagging false rate to half of its estimated value would shift the tagging efficiency to lie between 40% and 60%.

In conclusion the systematic effects points to the tagging efficiency and the tagging false rate not being known to high precision, but supports that the tagging efficiency is in the range of $50 \pm 10\%$, while the tagging false rate is below 1.1%.

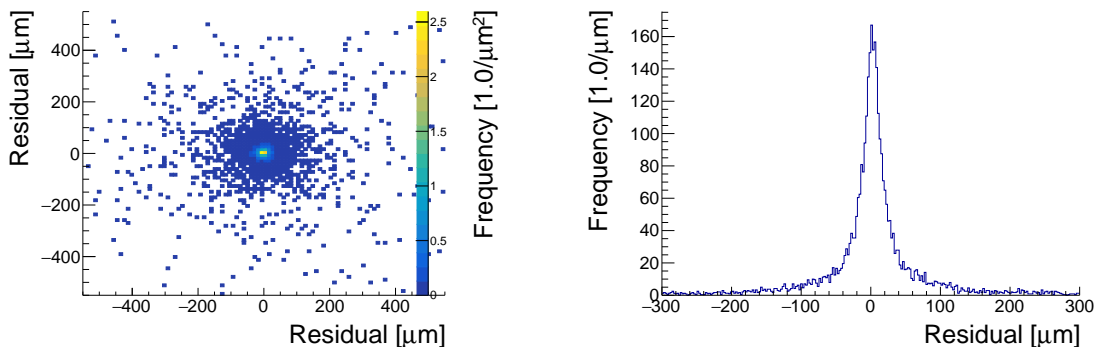# 6   Reconstruction of the annihilation point

This section uses the sample of simulated annihilation clusters to evaluate two methods for reconstructing the annihilation point: the mass center method and the vertex fitting method. Experiments for measuring the gravitational fall are expected to have low flux and therefore the pixels will in general have time to recover between being hit by different particles. For this reason the modeling of the suppressed pixels was excluded from this simulation. It was also assumed that the annihilation occurs in the central $5 \times 5 \, \mathrm{mm}^2$ of the detector such that prongs are not cut off by the edges of the detector. The relevant measurement for AEgIS is the vertical shift of the fringe pattern created by antihydrogen passing through the moiré deflectometer. Therefore the position resolution is calculated on the vertical direction y. The exact annihilation position is known from the simulation, and the residual is defined as the distance between the estimated annihilation point and the true annihilation point in the vertical direction. The metric chosen for position resolution is the symmetrical 68% confidence interval around 0 for the residuals, corresponding to $1.0 \, \sigma$ for a Gaussian distribution. This method of calculating the position resolution suppresses the effect of outliers.

6.1 Mass center method

The mass center method estimates the annihilation point by the weighted relative position of the energy depositions in the central region. The definition of the central region is found in section 2.3. Figures 13a and 13b show the result using the mass center method, and the position resolution is estimated to be 93 μm. This method can be applied to all clusters, as it does not require the presence of prongs.
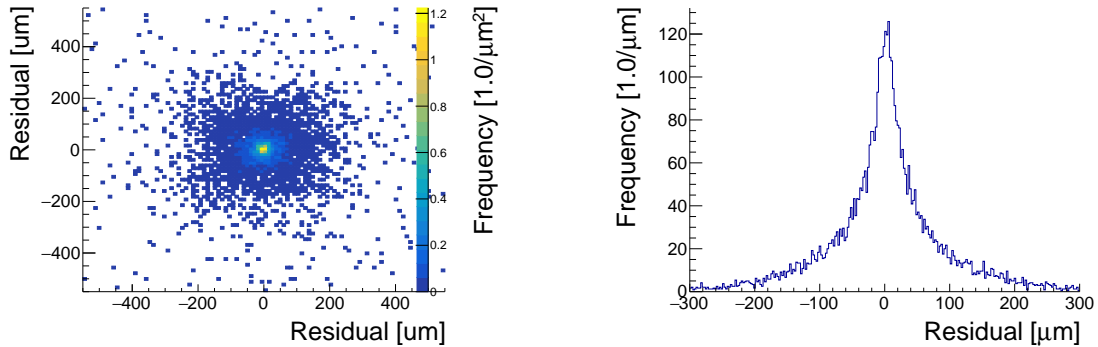
(a) Reconstructed annihilation point for antiprotons using the mass center method.

(b) Vertical distance between the fitted value and the true annihilation point using the mass center method. Estimated position resolution by 68% center is 93 μm.

(c) Reconstructed annihilation point for antiprotons using the vertex fitting method.

(d) Vertical distance between the fitted value and the true annihilation point using the vertex fitting method. Estimated position resolution by 68% center is 48 μm.

Figure 13. Position resolution using the mass center method and the vertex fitting method.

6.2 Vertex fitting method

The vertex fitting method fits straight lines to the prongs, and the annihilation point is taken as the intersection between two of these lines. The lines were fitted by the orthogonal-least-squares method. The vertex fitting method requires at least two prongs, and 45% of the clusters have two or more prongs.

Figure 14 shows how the residuals of the vertex fitting method correlate with the average number of pixels in the two prongs, the average length of the prongs, the crossing angle α between the two prongs, and the discrepancy of the estimates yielded by the two methods. According to figures 14a and 14b, the residuals are independent of the length of the prongs and the number of pixels in the prongs. That these two factors did not contribute to a better fit is probably because the same two factors also increases the probability that the prong undergoes scattering. The correlation between the residuals and the crossing angle shown in figure 14c shows that a crossing angle approaching parallel correlates with a bad fit, however the correlation is very weak and almost not visible in the scatter plot. Figure 14d shows the correlation between the discrepancy of the estimates from the two reconstruction methods and the residuals, and a strong correlation is evident for large residuals. This figure indicates that if the two methods disagree, the vertex fitting method is likely to give a bad estimate.

The following procedure was applied if there were more than two prongs yielding more than one candidate for the annihilation point. If two or more of the candidates are within a distance of $\pm 55\,\mu$m to each other the average of this cluster of candidates is taken as the estimate. If all candidates are separated by more than 55 μm, the one with its crossing angle closest to 90° is chosen since a crossing angle close to 90° correlates with a good fit. This method proved to be more robust than reconstructing to a common vertex since, in cases where there are more than two prongs, it is likely to exclude prongs that are not contributing to a good estimate. The result of the vertex fitting method is shown in figure 13c and 13d, and the vertical position resolution was improved from 93 μm to 48 μm compared to the mass center method.

In some situations it might be beneficial to select a smaller sub-sample of clusters that are known to yield better reconstructed values. The disagreement between the two methods indicates a bad fit, and therefore excluding clusters where the two methods don't agree can provide such a sub-sample of clusters that are more accurately reconstructed. Requiring the difference between the estimates from the two methods to be less than 110 μm, a sub-sample consisting of 22% of the clusters was selected, and in this sample a position resolution of 22 μm was obtained.

By resampling the MC data the statistical uncertainty is found to be only $\pm 0.5\,\mu$m. The achieved position resolution might also be subject to systematic errors caused by the simulation not fully reproducing experimental data. Assuming that this manifest itself in different spectra of annihilation products it is relevant to check how a a change in annihilation products affects the position resolution. Therefore the simulation and vertex reconstruction was also run with annihilations in carbon and calcium, as this respectively gives a higher and lower ratio of pions to nuclear fragments. The resulting position resolution is 21.3 μm for annihilation in carbon and 21.8 μm for annihilation in calcium. This gives an indication that systematic effects do not influence the position resolution to a large extent.

An absolute requirement for the position resolution is to be below the proposed 60 μm periodicity of the moiré deflectometer, and this requirement is met. Simulation studies have shown that a resolution of 10–13 μm is required to measure the gravitation acceleration with a precision of $\pm 1\%$. Even though this requirement is not met, the achieved position resolution should be good enough to perform a proof of principle measurement where a shift in the fringe pattern is observed [1].
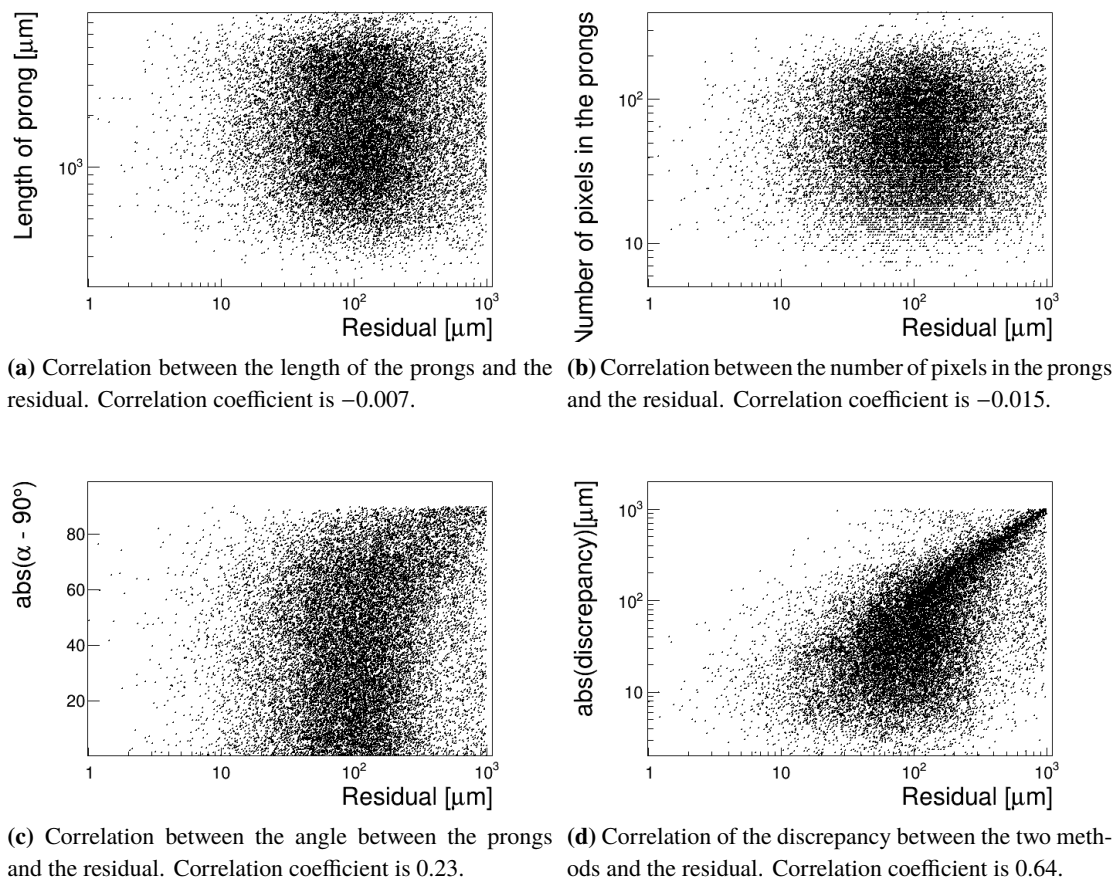
(a) Correlation between the length of the prongs and the residual. Correlation coefficient is −0.007.

(b) Correlation between the number of pixels in the prongs and the residual. Correlation coefficient is −0.015.

(c) Correlation between the angle between the prongs and the residual. Correlation coefficient is 0.23.

(d) Correlation of the discrepancy between the two methods and the residual. Correlation coefficient is 0.64.

Figure 14. Plots showing the correlation between prong parameters and the accuracy of the fit.

7 Conclusions

This work presents a detailed study of the annihilation of antiprotons with clear prongs in a thick Timepix3 detector. A full detector response model based on FLUKA was developed. The model was verified by comparison with experimental data, and it reproduces the geometrical variables such as cluster size and number of prongs quite well. An algorithm for characterizing and tagging the antiproton clusters was also developed. Applying this algorithm, a tagging efficiency of $50 \pm 10\%$ is estimated with cuts of at least 70 pixels and at least 1 prong, while the false tagging rate is 1% with the same cuts.

The detector response model was also used to investigate the possibility of reconstructing the annihilation point from linear fits to the prongs. With low flux, and thus few suppressed pixels, this proved to be possible for 22% of the clusters, and a vertical position resolution of $22 \pm 0.5\,\mu m$ was obtained. AEgIS expects to measure a vertical fall of $\approx 20\,\mu m$ over the length of 1 m, given that the antihydrogen beam has a velocity of less than 500 m/s. The position resolution obtained here is low enough for such a fall to be observed.

Acknowledgments

References

[1] G. Drobychev et al., *Proposal for the AEGIS experiment at the CERN antiproton decelerator (Antimatter Experiment: Gravity, Interferometry, Spectroscopy)*, CERN-SPSC-2007-017 (2007).

[2] AEGIS collaboration, *Exploring the WEP with a pulsed cold beam of antihydrogen*, *Class. Quant. Grav.* **29** (2012) 184009.

[3] S. Aghion et al., *A moiré deflectometer for antimatter*, *Nature Commun.* **5** (2014) 4538.

[4] M.K. Oberthaler, S. Bernet, E.M. Rasel, J. Schmiedmayer and A. Zeilinger, *Inertial sensing with classical atomic beams*, *Phys. Rev.* **A 54** (1996) 3165.

[5] AEGIS Proto collaboration, *Proposed antimatter gravity measurement with an antihydrogen beam*, *Nucl. Instrum. Meth.* **B 266** (2008) 351.

[6] M. Kimura et al., *Development of nuclear emulsions with 1 μm spatial resolution for the AEgIS experiment*, *Nucl. Instrum. Meth.* **A 732** (2013) 325.

[7] A. Gligorova et al., *Comparison of Planar and 3D Silicon Pixel Sensors Used for Detection of Low Energy Antiprotons*, *IEEE Trans. Nucl. Sci.* **61** (2014) 3747.

[8] T. Poikela et al., *Timepix3: a 65k channel hybrid pixel readout chip with simultaneous toa/tot and sparse readout*, 2014 *JINST* **9** C05013.

[9] N. Pacifico et al., *Direct detection of antiprotons with the timepix3 in a new electrostatic selection beamline*, *Nucl. Instrum. Meth.* **A 03** (2016) 12.

[10] P. Beloshitsky, T. Eriksson and S. Maury, *The CERN antiproton decelerator (AD) in 2002: Status, progress and machine development results*, *Nucl. Instrum. Meth.* **B 214** (2004) 176.

[11] G. Bendiscioli and D. Kharzeev, *Anti-nucleon nucleon and anti-nucleon nucleus interaction: A review of experimental data*, *Riv. Nuovo Cim.* **17N6** (1994) 1.

[12] S. Aghion et al., *Measurement of antiproton annihilation on Cu, Ag and Au with emulsion films*, 2017 *JINST* **12** P04021 [arXiv:1701.06306].

[13] T.T. Böhlen, F. Cerutti, M.P.W. Chin, A. Fassò, A. Ferrari, P.G. Ortega et al., *The FLUKA Code: Developments and Challenges for High Energy and Medical Applications*, *Nucl. Data Sheets* **120** (2014) 211.

[14] L. Tlustos, private communication (2017).

[15] C. Granja, J. Jakubek, U. Köster, M. Platkevic and S. Pospisil, *Response of the pixel detector timepix to heavy ions*, *Nucl. Instrum. Meth.* **A 633** (2011) S198.

[16] T.E.J. Campbell-Ricketts, M. Kroupa and L.S. Pinsky, *Spectroscopy of high-energy ions with timepix3*, 2016 *JINST* **11** P11007.

[17] J.S. Coursey, M.A. Zucker, M.J. Berger and J. Chang, *Estar pstar and astar: Computer programs for calculating stopping-power and range tables for electrons, protons, and helium ions*, (2005).

[18] N. Stoffle, L. Pinsky, S. Hoang, J. Idarraga, M. Kroupa, J. Jakubek et al., *Initial results on charge and velocity discrimination for heavy ions using silicon-Timepix detectors*, 2012 *JINST* **7** C12009.

[19] L. Pinsky, *Summary of medipix technology's 3-years in space and plans for future developments*, at *The 14th Vienna Converence on Instrumentation*, Vienna Austria (2016).

[20] R.O. Duda and P.E. Hart, *Use of the hough transformation to detect lines and curves in pictures*, *Commun. ACM* **15** (1972) 11.

[21] L. Rossi, P. Fischer, T. Rohe and N. Wermes, *Pixel Detectors: From Fundamentals to Applications*, Springer, Heidelberg Germany (2006).

[22] G. Lutz, *Semiconductor radiation detectors*, Springer, Heidelberg Germany (1999).

[23] K. Sjobak, *Full simulation of a testbeam experiment including modeling of the Bonn Atlas Telescope and Atlas 3D pixel silicon sensors*, MSc. Thesis, University of Oslo, Oslo Norway (2010).

[24] P.A. Tove and W. Seibt, *Plasma effects in semiconductor detectors*, *Nucl. Instrum. Meth.* **51** (1967) 261.

[25] https://www.synopsys.com/silicon/tcad.html, (2017).

[26] C.H. Wang, K. Misiakos and A. Neugroschel, *Minority-carrier transport parameters in n-type silicon*, *IEEE Trans. Electron Dev.* **37** (1990) 1314.